Energy-dependent contrast in atomic-scale spin-polarized scanning tunneling microscopy of Mn_3N_2 (010): Experiment and first-principles theory

Rong Yang,* Haiqiang Yang, and Arthur R. Smith†
Nanoscale and Quantum Phenomena Institute, Department of Physics and Astronomy, Ohio University, Athens, Ohio 45701, USA

Alexey Dick and Jörg Neugebauer
Max-Planck-Institut für Eisenforschung GmbH, Max-Planck Strasse 1, 40237 Düsseldorf, Germany
and Theoretische Physik, Universität Paderborn, Warburger Strasse 100, 33098 Paderborn, Germany
(Received 7 May 2005; revised manuscript received 13 July 2006; published 21 September 2006)

The row-wise antiferromagnetic Mn_3N_2 (010) surface has been investigated using atomic-scale spin-polarized scanning tunneling microscopy. Localizing the experimental image at a particular region of the surface, the bias voltage-dependent behavior and resulting energy-dependent magnetic contrast are investigated. It is found that the magnetic contrast varies strongly over the energy range from $E_{\mathrm{Fermi}}-1$ eV to $E_{\mathrm{Fermi}}+1$ eV, including a magnetic contrast reversal at $\sim E_{\mathrm{Fermi}}+0.4$ eV. Spin-polarized density-functional theory has been combined with the spin-generalized Tersoff-Hamann model to simulate the experimental results on Mn_3N_2 (010). Excellent agreement is found which shows that the observed bias-dependent behavior derives from the properties of the sample surface, not the tunneling tip. The bias-dependent contrast reversal, as well as bias-dependent line profile shape, are both found to result from a transition from majority (d_{z^2}) to minority (d_{yz}) spin-polarized Mn atomic orbital lobes.

DOI: 10.1103/PhysRevB.74.115409 PACS number(s): 68.37.Ef, 75.70.−i, 75.50.Ee, 75.70.Rf

I. INTRODUCTION

Nanoscale magnetism is a topic of increasing interest, having potential applications in advanced data storage and spin-based electronics. One of the most powerful techniques with the ability to probe magnetic structure at the nanoscale is spin-polarized scanning tunneling microscopy (SP-STM). This technique offers spin sensitivity combined with the well-known advantage of STM, namely, spatial resolution down to the atomic-scale. SP-STM has thus far been utilized to great advantage in imaging both ferromagnetic and antiferromagnetic surface structures.[1–11]

The principle of SP-STM is based on the variation of the tunneling current with the angle between the spin of the tip and that of the sample—larger current for parallel orientation and smaller current for antiparallel orientation. This effect depends on the local density of states for spin-↑ and spin-↓ channels. SP-STM has been used by Wiesendanger *et al.* to map the energy-dependent spin polarization of nanoscale ferromagnetic Gd(0001) islands by applying a magnetic field to the sample and measuring dI/dV versus V in the tip-sample parallel and antiparallel configurations.[2] For deriving the polarization in the case of an antiferromagnetic (AFM) surface, an external field is not required since the parallel and antiparallel configurations occur periodically as one moves the tip from row to row.

Regarding AFM surfaces, Heinze *et al.* reported the atomic-scale magnetic contrast of a Mn monolayer on a W(110) using atomic-scale SP-STM in constant current (CC) mode.[4] Two years later, Yang *et al.* showed the simultaneous magnetic and nonmagnetic contrast on Mn_3N_2 (010) using also atomic-scale SP-STM in CC mode.[5] Very recently, Kubetzka *et al.* have applied the same technique to study a single monolayer of Fe on W(001), resolving a long-standing question regarding the magnetic ground state of this system.[11] Atomic-scale SP-STM has therefore been established as a powerful technique for resolving the ultimate limits of magnetic structure on surfaces.

In this paper, we explore the effect of bias voltage on the magnetic corrugation on AFM Mn_3N_2 (010). The Mn_3N_2 (010) surface is a model AFM surface for such studies. The Mn atoms of the highly bulklike surface have magnetic moments that alternate in a row-wise AFM arrangement.[10,12] Bulk measurements show the corresponding layer-wise AFM structure with magnetic moments of Mn_1 and Mn_2, which are each close to $\sim 3.5\mu_B$,[13,14] and bulk theoretical calculations are in good agreement.[15] SP-STM corrugation profiles in general are found to contain both magnetic and nonmagnetic information. Here, it is found that the magnetic STM image depends strongly on the bias voltage, and at certain voltage the magnetic amplitude goes to zero. The bias voltage dependence is also found to affect the SP-STM line profile shape. Comparisons of the experimental SP-STM images and height profiles to simulated SP-STM images and height profiles calculated from spin-polarized first-principles density-functional theory are shown. Straightforward interpretation of the obtained results with emphasis on the magnetic contribution is made, based on the electronic properties of the Mn_3N_2 (010) surface.

II. EXPERIMENTAL APPROACH

The experiments are performed in a combined ultrahigh-vacuum (UHV) growth-analysis system that allows direct UHV transfer of samples from the growth chamber to the STM chamber. The MBE system includes a solid source effusion cell for Mn and a rf plasma source for N. After being heated up to 1000 °C for 30 min with the nitrogen plasma turned on, the MgO substrate temperature is lowered to 450 °C prior to the growth of manganese nitride

$Mn_3N_2(010)$ thin film. The nitrogen flow rate is about 1.1 sccm (growth chamber pressure is 1.1×10^{-5} Torr) with the rf power set at 500 W. The Mn flux is about $3.5\times10^{14}/cm^2$ s. The growth condition is monitored using reflection high-energy electron diffraction (RHEED).[14] Following growth, the samples are investigated with *in situ* SP-STM. For normal STM studies, we use electrochemically etched tungsten tips that are cleaned in the ultrahigh-vacuum chamber using electron bombardment. For SP-STM studies, we coat the cleaned tips with Fe at room temperature to a thickness of 5–10 monolayers (ML). Coated tips are magnetized in a small ~40 mT magnetic field directed perpendicular to the tip axis. SP-STM images are taken in the constant current (CC) mode at room temperature.

III. THEORETICAL APPROACH

In order to understand theoretically the magnetic surface structure of Mn_3N_2 (010), we have performed an *ab initio* study. To describe the SP-STM experiments, we have used the spin-polarized Tersoff-Hamann approach. The tunneling current can be expressed as[16]

$$I_t \sim \int dE g_v(E)[n^t(E-eV_{\text{bias}})n^s(\{\mathbf{R}_t\},E) + \mathbf{m}^t(E-eV_{\text{bias}})\cdot\mathbf{m}^s(\{\mathbf{R}_t\},E)]. \quad (1)$$

Here, $g_v(E)=f(E-E_F)-f(E-E_F-eV_{\text{bias}})$, f is the Fermi function, E_F is the Fermi energy of the sample, and $n^t(E)$, $\mathbf{m}^t(E)$, $n^s(\{\mathbf{R}_t\},E)$, $\mathbf{m}^s(\{\mathbf{R}_t\},E)$ are energy-dependent nonmagnetic and magnetic densities of states (DOS) of the tip and local densities of states (LDOS) of the sample at the tip position $\mathbf{R}_t$, respectively. Since the exact geometric, electronic, and magnetic properties of the tip used in the experiment are not known (and can even change during the experiment), the conventional approach is to assume a tip with an energy-independent DOS. Equation (1) can then be written as

$$I_t \sim \int dE g_v(E)[n^s(\{\mathbf{R}_t\},E) + P_t m^s(\{\mathbf{R}_t\},E)]. \quad (2)$$

Here, $m^s(\{\mathbf{R}_t\},E)=|\mathbf{m}^s(\{\mathbf{R}_t\},E)|$ and $-1.0\leq P_t\leq 1.0$ is the effective spin polarization of the tip. $g_v(E)$ has been calculated with thermal smearing $k_BT=0.025$ eV, which corresponds to experimental conditions.

The nonmagnetic $n^s(\{\mathbf{R}_t\},E)$ and magnetic $m^s(\{\mathbf{R}_t\},E)$ LDOS of the sample entering Eq. (2) have been calculated employing density-functional theory. *Ab initio* based multiscale library S/PHI/nX (Ref. 17) has been used for analysis of the calculated data and for simulation of the SP-STM profiles. To get accurate surface geometry and electronic structure, we have used a plane-wave norm-conserving pseudopotential approach as implemented in ABINIT.[18,19] Mn and N have been represented by Troullier-Martins pseudopotentials with $3d$, $4s$, $4p$ (Mn) and $2s$, $2p$ (N) states as valence. Nonlinear core correction has been included into the Mn pseudopotential. A plane-wave energy cutoff of 50 Ry and a $3\times1\times1(3\times1\times3)$ Monkhorst-Pack mesh for slab (bulk) have been found to give converged results with respect to bulk geometry and surface energies. The bulk geometry has been calculated fully accounting for internal relaxations of the atomic structure. To ensure convergence of the SP-STM corrugation maps with respect to the k-point sampling, the $12\times4\times1$ Monkhorst-Pack mesh has been used.

To estimate the importance of the exchange-correlation functionals, we have performed two series of calculations employing either the spin-LDA[20,21] or the spin-PBE approximations,[22] and cross-checked obtained data. We have found that both functionals provide qualitatively similar SP-STM profiles, with magnetic contrast reversal occurring at positive bias voltages. The lattice parameters and internal atomic coordinates calculated within the spin-PBE approximation are, however, in a better agreement with experiment[14] than that obtained within the spin-LDA functional (+1.5% and 1% for spin-PBE versus −2.5% and 7% for spin-LDA, respectively). In the rest of the paper, therefore, we restrict the discussion to results obtained within the spin-PBE exchange-correlation approximation.

The surface has been modeled by a repeated slab geometry with a slab thickness of six atomic layers. The surface unit cell is that of the magnetic structure, i.e, each layer contains six Mn and four N atoms. The surface geometry has been kept unrelaxed, since forces acting onto atoms in the topmost layer along the surface normal are found to be less than 5×10^{-3} H/Bohr. The slabs have been separated by a vacuum region of 12 Å. Convergence checks showed the chosen slab and vacuum thickness to give error bars in the surface energy of less then 0.5 meV/Å^2, and to be well converged with respect to simulated SP-STM corrugation profiles.

It is well known[10,23] that due to exponential decay of the wave functions into the vacuum, the reliable description of the surface LDOS at tip-surface separations exceeding ~3 Å is hardly feasible within the plane-wave basis set. To overcome this deficiency, we have employed the real-space approach to describe the vacuum region. The real-space approach is *exact* and is based on the projection of the wave functions from the plane-wave basis onto the real-space basis. The real-space basis functions are ideally suited to describe the vacuum region since they include the exponential decay of the wave functions with respect to the correct effective vacuum potential, and provide *exact* description of the surface LDOS at any tip-surface separation. The detailed description of the real-space method is given elsewhere.[23] In the case of the $Mn_3N_2(010)$ surface, the real-space basis is used at tip-surface distances larger than 2.5 Å; the plane-wave basis is used everywhere else.

All STM simulations have been performed with a bias-independent constant tunneling current $I_t(eV_{\text{bias}})=I_{\text{const}}$, to model the experimental constant current regime.

IV. RESULTS AND DISCUSSION

A. Magnetic contrast on Mn_3N_2 (010)

Previous work has elucidated the geometrical structure of the (010) surface, which is depicted in Fig. 1(a) in the top

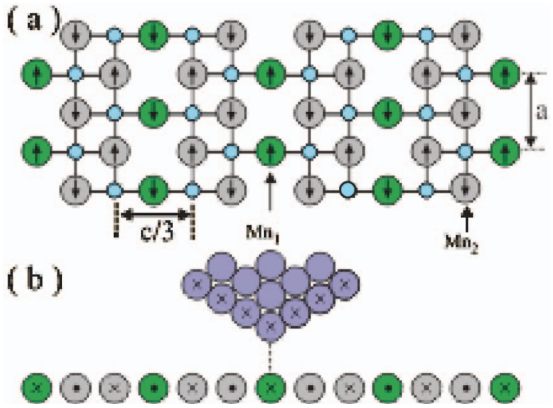

FIG. 1. (Color online) Top view of the bulk terminated surface model with magnetic moments indicated; (b) geometrical configuration of the SP-STM experiment. The cross and dot represent the directions of the magnetic moments.

view.[14] The surface is composed of Mn atoms in a face-centered tetragonal structure. There are two types (configurations) of surface Mn atoms: Mn_1, which has two in-plane bonds to N; and Mn_2, which has three in-plane bonds to N. Since the bulk c planes are layerwise antiferromagnetic and the c axis is in the surface plane, the surface atom magnetic moments alternate in a row-wise AFM arrangement. The atomic row-spacing along [001] is 2.02 Å whereas the row-spacing along [100] is 2.10 Å. The corresponding calculated values are 2.06 and 2.13 Å, respectively. Figure 1(b) illustrates the geometrical configuration for the SP-STM experiment.

Experimental CC-mode SP-STM images of the Mn_3N_2 (010) surface have been obtained, as shown in Fig. 2. This image is of size 100 Å × 100 Å with tunneling current I_t =0.3 nA and at sample bias voltage V_S=−0.2 V. The image shows the row structure of the Mn_3N_2 (010) surface; the spacing of the rows is 6.07 Å, which is equal to $c/2$ or 3 single atomic rows. The row spacing is therefore that between rows of Mn_1 atoms. A number of defects, probably Mn_1 vacancies, are observed on the surface. Although chemically all the Mn_1 rows are the same, a uniform modulation of the row heights is seen, which is due to the spin-polarized effect.[5] Since the STM is operated at constant current, the tip has to withdraw from or come closer to the surface depending on the magnetization directions of tip and sample. For Cr(001), this led to an alternation of the apparent step height.[1] For a row-wise AFM surface, the CC mode leads to the periodic modulation of the peak heights. The period of the magnetic modulation is two Mn_1 rows, or c=12.14 Å.

B. Analysis of the bias dependence of the magnetic contrast

Figures 3(a)–3(e) and 4(a)–4(e) show sets of CC modes SP-STM images acquired from the exact same location on the surface, namely from the boxed region shown in Fig. 2 (we used the defects on the surface to locate the position). As with the larger image shown in Fig. 2, these STM images do not resolve the individual Mn_1 and Mn_2 atoms; this is common for all of our spin-polarized STM images of this surface. It suggests that the magnetic tips are less sharp than a single atom tip. Note that we have published a complete study of the bias dependence of the atomic-resolution nonmagnetic images acquired with a sharp (possibly single atom) nonmagnetic tip.[12] In that data set, the Mn_1 and Mn_2 atoms are clearly resolved. Although there is no Mn_1 and Mn_2 atom resolution in the data shown here, we employed in our simulations the single atom tip model since the exact geometry of the tip apex is not known.

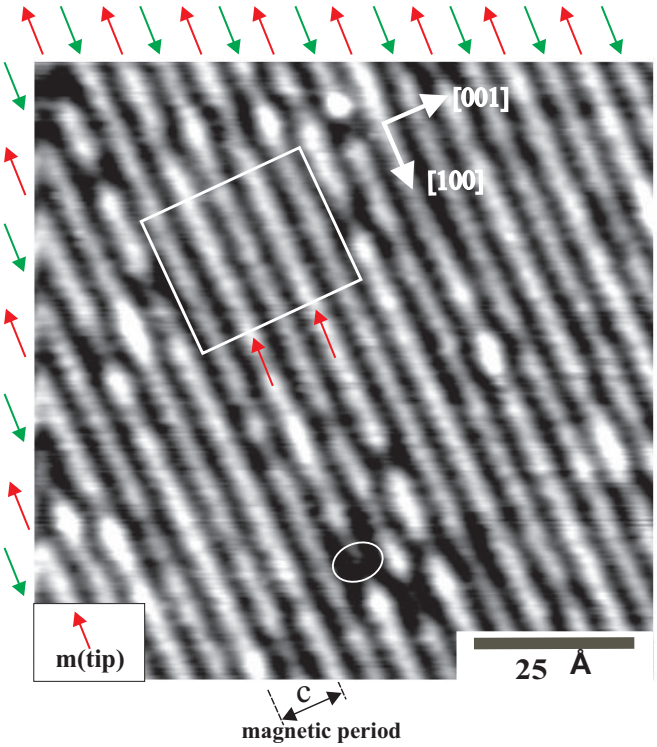

FIG. 2. (Color online) SP-STM image of Mn_3N_2 (010) surface acquired at V_s=−0.2 V and I_t=0.3 nA using an Fe-coated W tip; up arrows correspond to the bright rows, down arrows correspond to the less bright rows. The ellipse indicates one of the defect regions. The gray scale is 0.28 Å.

The [100]-averaged height profiles are also shown below each image and on the same scale throughout, where the height modulation of the rows as well as the overall corrugation can be clearly observed. What we find from these images is that there are distinct variations of the line profile as a function of energy, and several key points can be made. First, the overall corrugation magnitude is largest at the smallest bias magnitudes; we note that this trend is consistent with the atomic-resolution bias-dependent images.[12] Second, the magnetic modulation reaches a maximum of ~0.04 Å at V_S=−0.1 V. Third, magnetic modulation is observed clearly at all energies except at $V_S \sim +0.4$ V, where it becomes very small. In fact, and as the fourth key point, at $V_S \sim +0.4$ V the modulation undergoes a reversal. This magnetic contrast reversal is clear by counting the number of "high peaks" and "low peaks." For $V_s < 0.4$ V, there are two high peaks (indicated by upward arrows in Figs. 3 and 4) and three low peaks, whereas for $V_s > 0.4$ V, there are three high peaks and two low peaks.

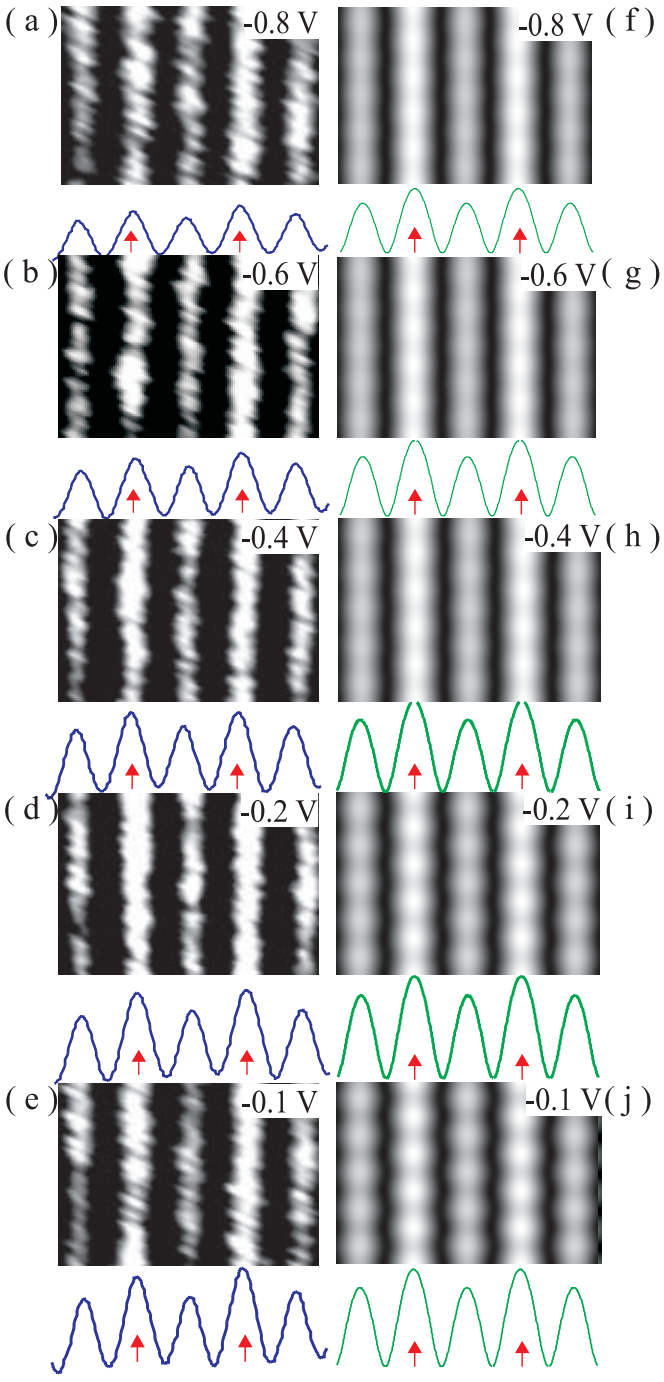

FIG. 3. (Color online) Experimental and theoretical SP-STM images for negative bias voltages. (a)–(e) A series of SP-STM images acquired using a Fe-coated W tip corresponding to the same box region in Fig. 2, with corresponding height line profiles. V_s from −0.8 to −0.1 V, and I_t=0.3 nA. (f)–(j) Corresponding theoretical images calculated using spin-polarized DFT assuming tip with constant DOS. All the line profiles are in the same scale. The maximum height profile magnitude is 0.28 Å.

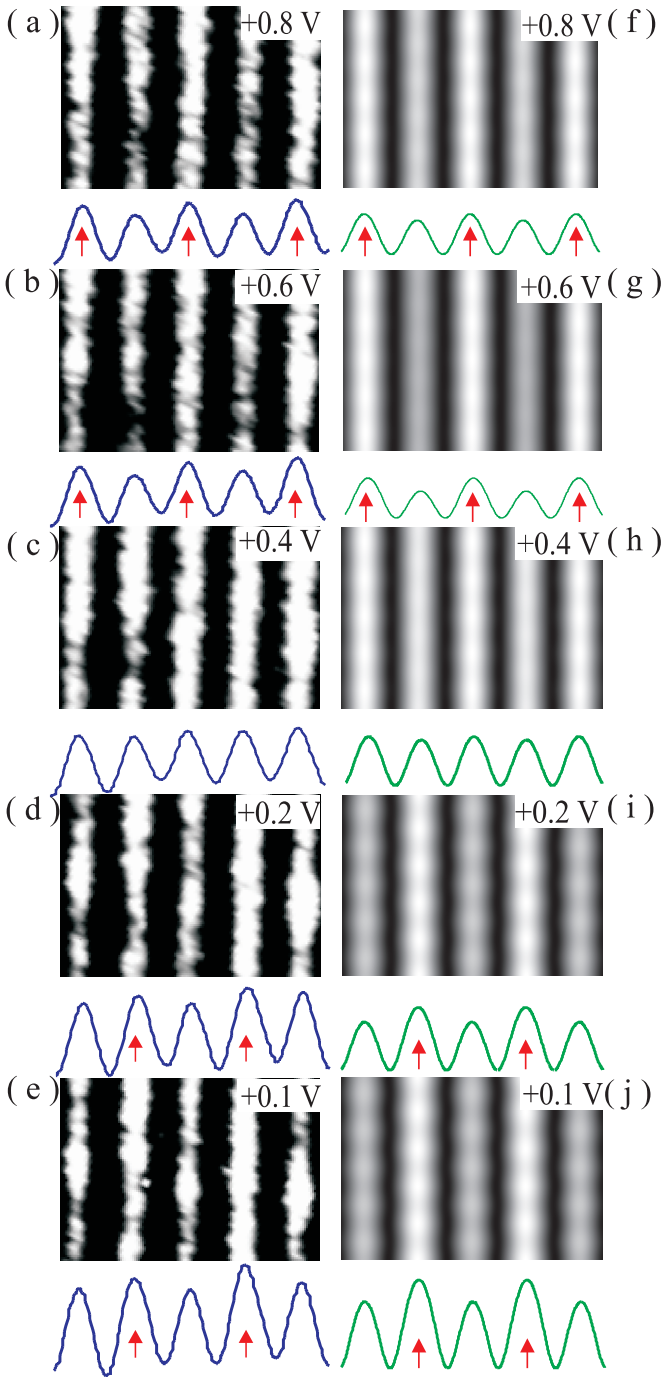

FIG. 4. (Color online) Experimental and theoretical SP-STM images for positive bias voltages. (a)–(e) A series of SP-STM images acquired using a Fe-coated W tip corresponding to the same box region in Fig. 2, with corresponding height line profiles. V_s from +0.1 to +0.8 V, and I_t=0.3 nA. (f)–(j) Corresponding theoretical images calculated using spin-polarized DFT assuming tip with constant DOS. All the line profiles are in the same scale. The maximum height profile magnitude is 0.28 Å.

We have separated the magnetic and nonmagnetic components from the total SP-STM experimental height profiles. This is done by adding and subtracting, for a given image, the averaged line profile and the same line profile shifted by half the magnetic period=$c/2$, as explained in more detail elsewhere.[5] The results are shown in Figs. 5(a)–5(e) and 6(a)–6(e) for each image corresponding to Figs. 3(a)–3(e) and 4(a)–4(e). It is clear that at all energies, the nonmagnetic component has a smooth sinusoidlike shape.

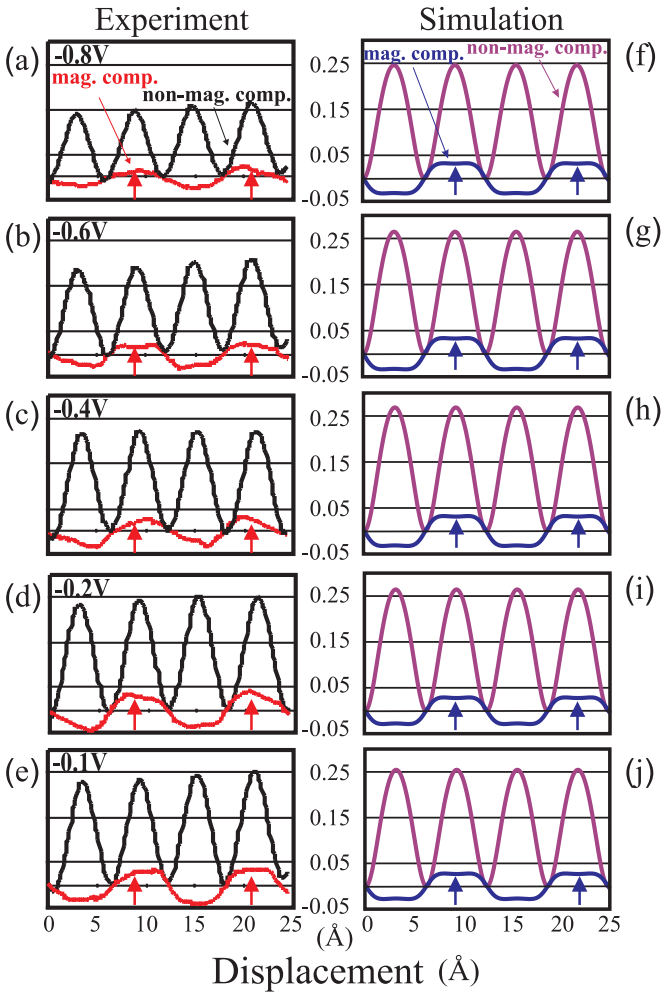

FIG. 5. (Color online) Resulting magnetic and nonmagnetic height profiles for negative bias voltages. (a)–(e) Experimental nonmagnetic and magnetic profiles. (f)–(j) Corresponding theoretical nonmagnetic and magnetic height profiles calculated using spin-polarized DFT assuming tip with constant DOS.

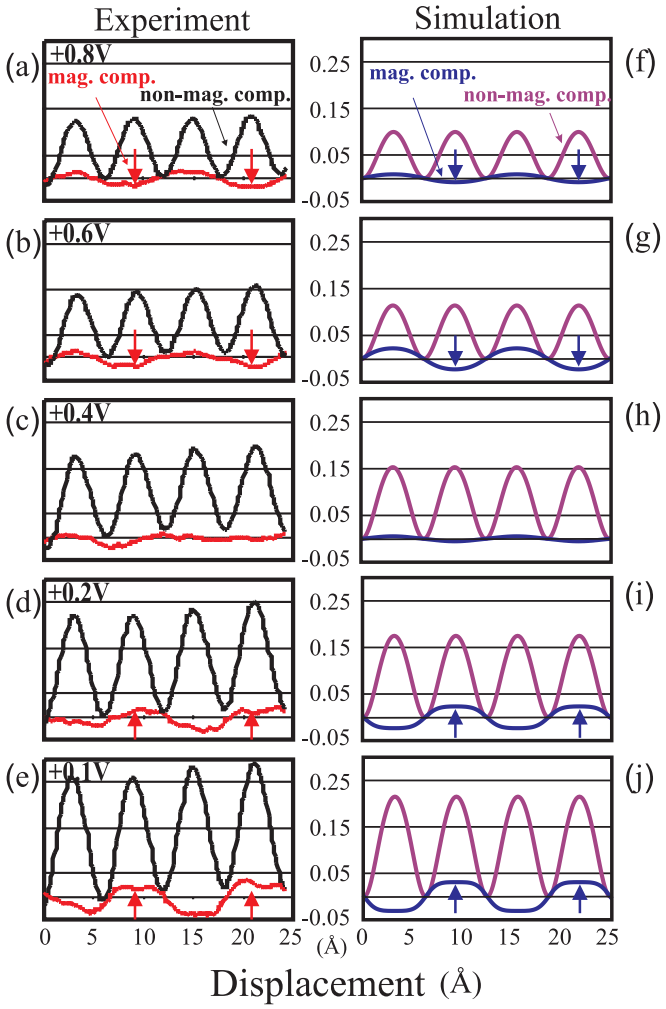

FIG. 6. (Color online) Resulting magnetic and nonmagnetic height profiles for positive bias voltages. (a)–(e) Experimental nonmagnetic and magnetic profiles. (f)–(j) Corresponding theoretical nonmagnetic and magnetic height profiles calculated using spin-polarized DFT assuming tip with constant DOS.

On the other hand, the magnetic component has a shape that varies with the energy. While to first order, the magnetic profile shape is roughly sinusoidal, at many voltages within the range from −0.8 to +0.2 V the magnetic profile shows a distinctly trapezoidlike shape. This is very clear at, for example, −0.6 and −0.2 V in Fig. 5. At positive voltages greater than 0.2 V, this trapezoidal shape is not evident; the profile is more rounded. Of course, at $V_S \sim 0.4$ V, the magnetic line profile is nearly flat, and the contrast reversal is near that point.

C. Explanation for magnetic contrast reversal

To analyze the SP-STM experiments, we have modeled the bias-dependent profiles using Eq. (2) and employing the conventional assumption of a constant (with energy) tip density of states, as was done, e.g., in Refs. 2, 7, and 24, where it was assumed that Fe tips have constant polarizations over the range from −0.5 to +0.5 eV of ~40%. Shown in Figs. 3(f)–3(j) and 4(f)–4(j) are the simulated SP-STM images obtained for a tip with constant *effective* polarization $P_t = 15\%$. The corresponding change of the averaged tip-surface separation versus applied bias voltage, which is dictated by the constant tunneling current regime, is shown in Fig. 7(a).

The simulations are for a surface region identical to the one in the experiment [Figs. 3(a)–3(e) and 4(a)–4(e)]. First of all, we find remarkable qualitative agreement between simulated SP-STM images and experimental SP-STM images: it is clearly apparent that both simulated and experimental images show magnetic contrast at all bias voltages with contrast reversal occurring at V_S near +0.4 V. Moreover, at positive bias voltages the overall corrugation of the simulated profiles is also largest at small bias magnitudes, whereas it is smaller at larger bias magnitudes, in agreement with the experiment. Similar behavior is observed at negative biases, with the exception of bias magnitudes smaller than 0.2 V (0.3 V) where the overall corrugation of the measured (simulated) profiles increases with increase of the $|V_S|$.

Similar to experiment, we have also separated the magnetic and nonmagnetic components from the total SP-STM

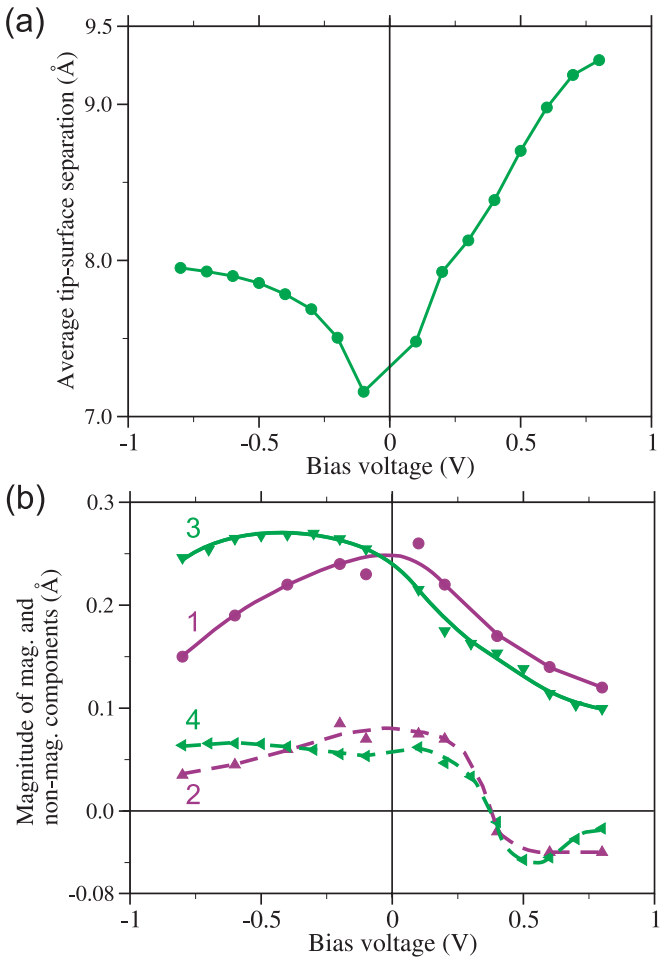

FIG. 7. (Color online) (a) Theoretical averaged tip-surface separation vs applied bias voltage. (b) The magnitude of magnetic component (triangles up, expt.; triangles left, theory) and nonmagnetic component (purple circles, expt.; triangles down, theory). Fitted solid and dashed curves 1-2 (expt.) and solid and dashed curves 3-4 (theory) are shown to guide eye.

theoretical height profiles. Figures 5(f)–5(j) and 6(f)–6(j) are the height profiles corresponding to the simulated SP-STM images shown in Figs. 3(f)–3(j) and 4(f)–4(j), respectively. Comparing nonmagnetic profiles with the experimental ones, we find that both agree well showing a simple sinusoidlike form. The magnetic profiles also are in perfect agreement with experiment for the whole range of biases between −0.8 and +0.8 V. Even the shape of the simulated magnetic profiles is in remarkable agreement with experiment, being trapezoidal below +0.4 V and more rounded above this value.

The experimental and theoretical magnetic and nonmagnetic line profile magnitudes (peak to valley) are plotted versus V_s in Fig. 7(b). Clearly, the magnitudes of the experimental nonmagnetic contributions [Fig. 7(b), curve 1] are maximum at small voltage, whereas they get smaller at larger magnitudes of voltage. The exception from this behavior is the magnitude of the nonmagnetic profile at −0.1 V, which is smaller than that at −0.2 V. For the experimental magnetic component [Fig. 7(b), curve 2], the sign change can be clearly seen at +0.4 V, indicating the change of polarity of the magnetic contrast.

The corresponding theoretical nonmagnetic and magnetic line profile magnitudes are also shown in Fig. 7(b) (curves 3 and 4, respectively). Qualitatively the magnitudes of the nonmagnetic contribution (curve 3) are in perfect agreement with experiment, smoothly decreasing with increase of the bias magnitude. In agreement with experiment, the exception from this behavior is at small negative biases. Quantitatively, the magnitudes of the simulated nonmagnetic profiles are slightly underestimated at positive biases, and overestimated at negative ones, with the largest deviation at V_S=−0.8 V. The simulated magnetic component (curve 4) is in perfect qualitative and quantitative agreement with the experiment (curve 2).

From comparative analysis of the simulated and experimental data in Figs. 3–7, it follows that even employing the simplest Tersoff-Hamann tip with constant DOS, it is possible to reproduce the whole set of experiments, with fairly good agreement for the magnetic part of the SP-STM profiles. We note here that to achieve better quantitative agreement for the nonmagnetic part (which is beyond the scope of the current study), one might need more precise information regarding the experimental tip geometrical and electronic properties.

Since the simulated profiles correspond to an electronically featureless tip, i.e., depend only on the surface electronic properties, we conclude that the experimentally observed magnetic contrast reversal can be adequately described solely in terms of the surface electronic structure.

In Fig. 8, the contour plots of the surface spin LDOS corresponding to different applied bias voltages are shown. Only positive voltages relevant to the magnetic contrast reversal are presented. First, comparing the magnetic LDOS in the energy range between +0.35 and +0.80 V, it is obvious that the magnetic contrast undergoes reversal: while at +0.35 V the spin-up density accumulates in the vicinity of the $Mn_1\downarrow$ rows (see Fig. 8), at +0.80 V this region is dominated by spin-down density. For biases close to +0.40 V, there is an apparent dependence of the surface magnetic LDOS on the distance above the surface. Specifically, at +0.4 V the inverse of the magnetic contrast occurs at ~7 Å above the surface: for distances smaller than ~7 Å, the magnetic LDOS behaves similar to that at +0.35 V, but above this distance the magnetic profile is essentially like at +0.80 V. For +0.45 V, the corresponding contrast reversal occurs at ~5 Å. The position of the contrast reversal plane thus depends on the bias voltage, therefore the voltage at which the magnetic contrast reversal occurs can vary slightly depending on the actual tip-surface separation.

To elucidate the origin of the magnetic contrast reversal, we have projected the surface electron wave functions onto localized atomic orbitals. We have found that the spin-density contribution stemming from the Mn_1 atoms is mainly of the minority (with respect to the total magnetic moment of the corresponding atom) d_{xz} character, and remains essentially unchanged at all relevant positive biases. The Mn_1 atoms, therefore, cannot be responsible for the magnetic contrast reversal.

On the other hand, there is an evident bias dependency of the Mn_2 electronic properties. At small positive bias

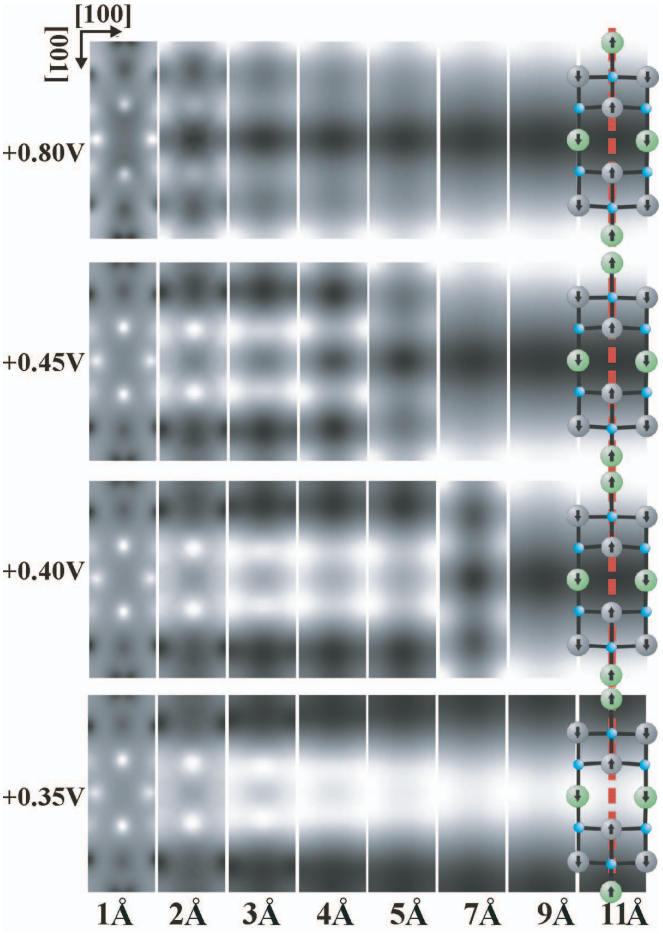

FIG. 8. (Color online) Evolution of the calculated surface spin-LDOS vs applied bias voltage (vertical axis) at different distances above the surface (horizontal axis). Bright and dark regions correspond to spin-up and spin-down densities correspondingly. Position of the top surface atoms is schematically shown on 11 Å plots. Arrows inside Mn_1 and Mn_2 atoms indicate their total magnetic moments; nitrogen atoms are shown as small balls. Dashed line along [001] direction corresponds to the position of the (100) cross-section planes shown in Fig. 9.

voltages, these atoms have predominant majority d_{z^2} character. These d_{z^2} orbitals are clearly distinguishable, e.g., in Fig. 8 as intense spots located on top of the Mn_2 atoms at ~1–2 Å above the surface, and in Fig. 9(c). Since the Mn_2-Mn_1-Mn_2 rows of surface atoms are row-wise AFM, the minority contribution of Mn_1 atoms is of the same sign as the majority contributions of the surrounding Mn_2 atoms. The overlap of the minority d_{xz} lobes of Mn_1 atoms with the majority d_{z^2} lobes of the surrounding Mn_2 atoms results, therefore, in the total $(\uparrow\uparrow\uparrow)(\downarrow\downarrow\downarrow)$ pattern at all distances above the surface, as shown at +0.35 V in Fig. 8.

As bias voltage V_S increases, the spin character of Mn_2 atoms evolves smoothly from the majority d_{z^2} to minority d_{yz}. This can be seen in Fig. 9 at +0.5 and +0.8 V, where the minority d_{yz} orbital lobes become more prominent. These lobes tend to overlap on top of the neighboring Mn_1 row above the hollow site positions. At sufficiently large bias voltages, the minority d_{yz} of the Mn_2 atoms effectively

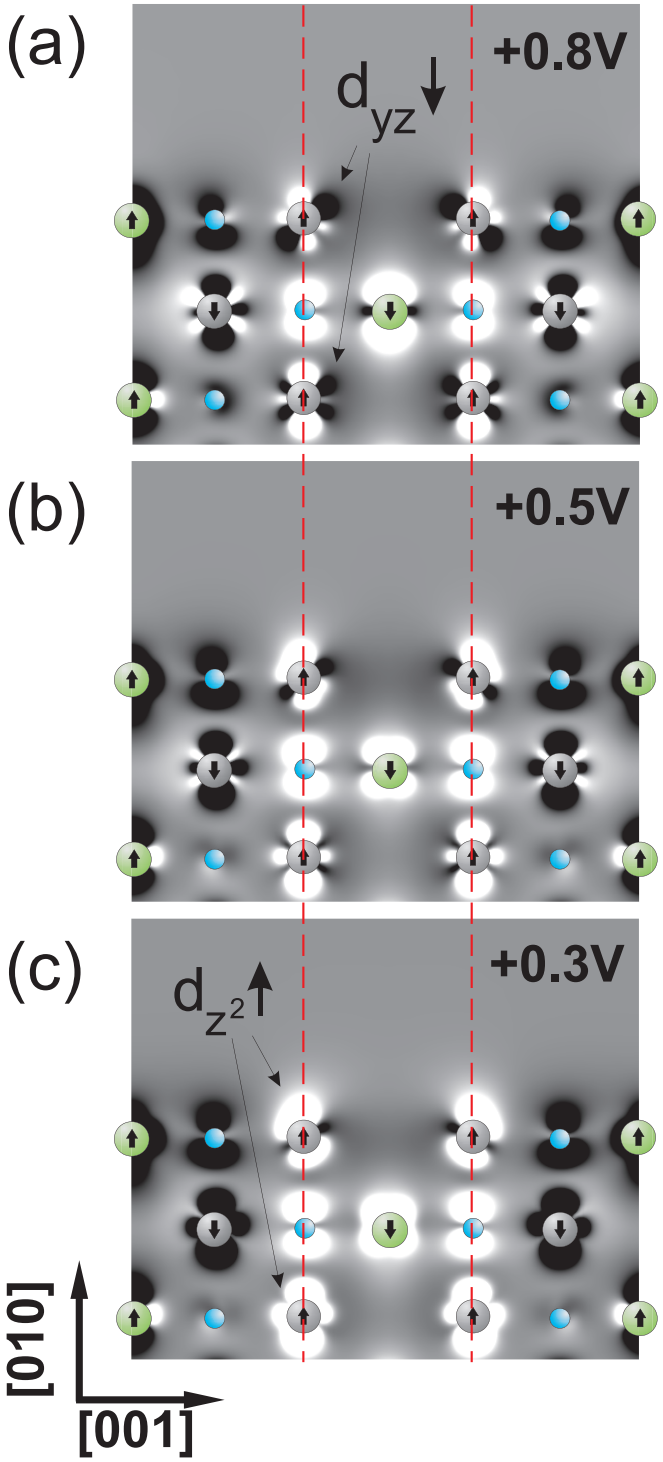

FIG. 9. (Color online) Evolution of the calculated surface spin density with change of the bias voltage. Cross sections in the (100) plane corresponding to bias voltage +0.8 V (a), +0.5 V (b), and +0.3 V (c) are shown; the position of the cross section with respect to the surface unit cell is depicted in Fig. 8 as a vertical dashed line. Arrows inside Mn_1 and Mn_2 atoms indicate their total magnetic moments; nitrogen atoms are shown as small balls. Bright and dark regions correspond to spin-up and spin-down densities correspondingly. Vertical dashed lines indicate rows of Mn_2 atoms that effectively screen contribution of Mn_1 atoms located in between.

screens the minority d_{xz} of the Mn_1 atoms and becomes dominating in the surface spin LDOS. This is manifested by the appearance of the high spin-density features on the hollow sites in the Mn_1 rows (see, e.g., the spin-LDOS at +0.8 V in Fig. 8), and leads to the inverse of the magnetic pattern, e.g., from (↑↑↑) to (↓↓↓) and vice versa.

The magnetic contrast reversal at the $Mn_3N_2(010)$ surface is, therefore, caused by the smooth change from majority to minority d orbitals of the Mn_2 atoms occurring above the Fermi level. At sufficiently large positive biases, this leads to an effective (↓↓↓)(↑↑↑) magnetic pattern with underlying (Mn_2↑Mn_1↓Mn_2↑)(Mn_2↓Mn_1↑Mn_2↓) rows of manganese atom moments.

Finally, it is not coincidental that the change in magnetic line profile shape from trapezoidal to rounded, observed in both experiment and theory, occurs at about the same bias voltage as the magnetic contrast reversal, namely at $V_S \sim +0.4$ V. In fact, the line profile shape transition can also be explained by the change from majority to minority d orbitals. As can be seen from Fig. 9, at +0.3 V the majority d_{z^2} orbital lobes of the 2 Mn_2 surface atoms are relatively far apart, leading to the trapezoidal-like line profile shape. But as voltage increases (i.e., as seen at +0.5 and +0.8 V), the minority d_{yz} orbital lobes become more prominent and, since they are spatially closer together, lead to the more rounded line profile. As a concluding remark, we note that the aforementioned smooth change from majority d_{z^2} to minority d_{yz} electronic character for Mn_2 atoms at the surface is dictated by the underlying AFM bulk structure. This is supported by our analysis of the surface and bulk projected density of states and can also be seen, e.g., in Fig. 9. There, an increase of the bias leads to essentially identical changes for surface and bulk Mn_2 atoms. In this way, the observed inversion of the magnetic contrast reflects the underlying bulk electronic properties.

V. SUMMARY

In summary, we have analyzed the bias-dependent magnetic profiles obtained by SP-STM on a model AFM surface at room temperature. Particularly, we have shown that a polarization reversal occurs and that the magnetic contrast and magnetic line profile shape vary with the bias voltage. Based on our spin-polarized DFT calculations, we have performed simulations of the SP-STM experiments employing a featureless STM tip model. Our theoretical results are in very good agreement with measured profiles and allow one to interpret the observed reversal of the magnetic contrast as a surface-driven, rather than tip-driven, effect. Moreover, the change in line profile shape, as well as the magnetic contrast reversal, are each explained in terms of the smooth change from majority to minority spin d orbitals.

ACKNOWLEDGMENTS

This work has been supported by the National Science Foundation under Grants No. 9983816 and 0304314.

*Email address: yang@helios.phy.ohiou.edu
†Email address: smitha2@ohio.edu

[1] R. Wiesendanger, H.-J. Guntherodt, G. Guntherodt, R. J. Gambino, and R. Ruf, Phys. Rev. Lett. **65**, 247 (1990).
[2] R. Wiesendanger, M. Bode, and M. Getzlaff, Appl. Phys. Lett. **75**, 124 (1999).
[3] M. Kleiber, M. Bode, R. Ravlic, and R. Wiesendanger, Phys. Rev. Lett. **85**, 4606 (2000).
[4] S. Heinze, M. Bode, A. Kubetzka, O. Pietzsch, X. Nie, S. Blügel, and R. Wiesendanger, Science **288**, 1805 (2000).
[5] H. Yang, A. R. Smith, M. Prikhodko, and W. R. L. Lambrecht, Phys. Rev. Lett. **89**, 226101 (2002).
[6] S. N. Okuno, T. Kishi, and K. Tanaka, Phys. Rev. Lett. **88**, 066803 (2002).
[7] M. Bode, M. Getzlaff, and R. Wiesendanger, Phys. Rev. Lett. **81**, 4256 (1998).
[8] T. K. Yamada, M. M. J. Bischoff, G. M. M. Heijnen, T. Mizoguchi, and H. van Kempen, Phys. Rev. Lett. **90**, 056803 (2003).
[9] A. Kubetzka, O. Pietzsch, M. Bode, and R. Wiesendanger, Appl. Phys. A **76**, 873 (2003).
[10] A. R. Smith, R. Yang, H. Q. Yang, W. R. L. Lambrecht, A. Dick, and J. Neugebauer, Surf. Sci. **561**, 154 (2004).
[11] A. Kubetzka, P. Ferriani, M. Bode, S. Heinze, G. Bihlmayer, K. von Bergmann, O. Pietzsch, S. Blügel, and R. Wiesenganger, Phys. Rev. Lett. **94**, 087204 (2005).
[12] H. Q. Yang, R. Yang, A. R. Smith, and Walter R. L. Lambrecht, Surf. Sci. **548**, 117 (2004).
[13] A. Leineweber, R. Niewa, H. Jacobs, and W. Kockelmann, J. Mater. Chem. **10**(12), 2827 (2000).
[14] H. Q. Yang, H. Al-Brithen, A. R. Smith, J. A. Borchers, R. L. Cappelletti, and M. D. Vaudin, Appl. Phys. Lett. **78**, 3860 (2001).
[15] W. R. L. Lambrecht, M. Prikhodko, and M. S. Miao, Phys. Rev. B **68**, 174411 (2003).
[16] D. Wortmann, S. Heinze, Ph. Kurz, G. Bihlmayer, and S. Blügel, Phys. Rev. Lett. **86**, 4132 (2001).
[17] http://www.sxlib.de
[18] X. Gonze, J.-M. Beuken, R. Caracas, F. Detraux, M. Fuchs, G.-M. Rignanese, L. Sindic, M. Verstraete, G. Zerah, F. Jollet, M. Torrent, A. Roy, M. Mikami, Ph. Ghosez, J.-Y. Raty, and D. C. Allan, Comput. Mater. Sci. **25**, 478–492 (2002).
[19] X. Gonze, G.-M. Rignanese, M. Verstraete, J.-M. Beuken, Y. Pouillon, R. Caracas, F. Jollet, M. Torrent, G. Zerah, M. Mikami, Ph. Ghosez, M. Veithen, J.-Y. Raty, V. Olevano, F. Bruneval, L. Reining, R. Godby, G. Onida, D. R. Hamann, and D. C. Allan, Z. Kristallogr. **220**, 558 (2005).
[20] J. P. Perdew and A. Zunger, Phys. Rev. B **23**, 5048 (1981).
[21] J. P. Perdew and Y. Wang, Phys. Rev. B **45**, 13244 (1992).
[22] J. P. Perdew, K. Burke, and Y. Wang, Phys. Rev. B **54**, 16533 (1996).
[23] S. Heinze, S. Blugel, R. Pascal, M. Bode, and R. Wiesendanger, Phys. Rev. B **58**, 16432 (1998).
[24] P. M. Tedow and R. Meservey, Phys. Rev. B **7**, 318 (1973).